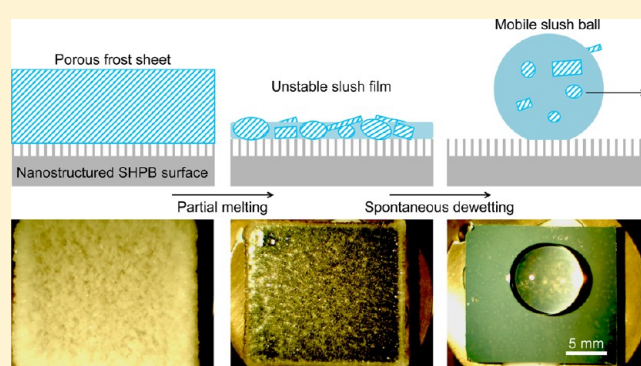


## Dynamic Defrosting on Nanostructured Superhydrophobic Surfaces

Jonathan B. Boreyko,<sup>†</sup> Bernadeta R. Srijanto,<sup>†,‡</sup> Trung Dac Nguyen,<sup>‡</sup> Carlos Vega,<sup>||</sup> Miguel Fuentes-Cabrera,<sup>†,§</sup> and C. Patrick Collier<sup>\*,†</sup><sup>†</sup>Center for Nanophase Materials Sciences, <sup>‡</sup>National Center for Computational Sciences, and <sup>§</sup>Computer Science and Mathematics Division, Oak Ridge National Laboratory, Oak Ridge, Tennessee 37831, United States<sup>||</sup>Departamento de Química Física, Facultad de Ciencias Químicas, Universidad Complutense, 28040 Madrid, Spain<sup>‡</sup>Department of Materials Science & Engineering, University of Tennessee, Knoxville, Tennessee 37996, United States

## Supporting Information

**ABSTRACT:** Water suspended on chilled superhydrophobic surfaces exhibits delayed freezing; however, the interdrop growth of frost through subcooled condensate forming on the surface seems unavoidable in humid environments. It is therefore of great practical importance to determine whether facile defrosting is possible on superhydrophobic surfaces. Here, we report that nanostructured superhydrophobic surfaces promote the growth of frost in a suspended Cassie state, enabling its dynamic removal upon partial melting at low tilt angles ( $<15^\circ$ ). The dynamic removal of the melting frost occurred in two stages: spontaneous dewetting followed by gravitational mobilization. This dynamic defrosting phenomenon is driven by the low contact angle hysteresis of the defrosted meltwater relative to frost on microstructured superhydrophobic surfaces, which forms in the impaled Wenzel state. Dynamic defrosting on nanostructured superhydrophobic surfaces minimizes the time, heat, and gravitational energy required to remove frost from the surface, and is of interest for a variety of systems in cold and humid environments.



## 1. INTRODUCTION

The accretion of frost on infrastructure including aircraft, marine structures, power grids, wind turbines, and HVAC systems can heavily compromise both their mechanical integrity and energy efficiency. For example, the heating capacity of an air source heat pump decreases by about 30% after an hour of frost growth on the outdoor heat exchanger.<sup>1</sup> When defrosting traditional surfaces, the meltwater remains wetted to the substrate and must be evaporated at high temperatures (or imperfectly drained when utilizing a vertical orientation). When defrosting a heat pump, for example, the compressor's suction temperature increases from  $-2$  to  $30$  °C while the discharge temperature decreases from  $80$  to  $40$  °C over a span of about 5 min, during which time the heat pump's coefficient of performance (COP) decreases from 3 to about 0.2.<sup>2</sup> It is therefore of immense practical interest to investigate whether defrosting could be accomplished at faster time scales and at lower temperatures.

Over the past decade, much interest has been generated in utilizing superhydrophobic surfaces for anti-ice and antifrost applications.<sup>3</sup> Water on roughened superhydrophobic surfaces typically exhibits a suspended Cassie state, where the water is largely insulated from the surface by an intermediate air layer.<sup>4</sup> Under subzero conditions, this results in delayed freezing due to the reduced liquid–solid contact minimizing both the heat transfer rate<sup>5,6</sup> and the probability of heterogeneous ice

nucleation<sup>7–11</sup> compared to traditional surfaces. While the freezing of sessile drops is delayed but still inevitable, the low contact angle hysteresis of a superhydrophobic surface can be exploited to gravitationally remove drops via sliding<sup>6</sup> and/or rebounding<sup>8</sup> before ice nucleation can occur.

However, when condensation nucleates on superhydrophobic surfaces due to ambient humidity, it is well-known that the condensate drops typically form in the impaled Wenzel state.<sup>12,13</sup> In subzero conditions, this Wenzel condensate freezes over into a sheet of frost that is impaled within the surface roughness of the superhydrophobic surface. Therefore, most superhydrophobic surfaces have been reported to actually increase the adhesion of frost compared to traditional (flat) surfaces.<sup>14–16</sup> Even if this frost sheet was melted back into liquid, it has been previously reported that fully impaled Wenzel drops are incapable of a dewetting transition to the mobile Cassie state even when mechanically forced.<sup>17</sup> To date, the outlook for utilizing superhydrophobic surfaces for facile defrosting has not seemed promising.

Very recently, it has been found that superhydrophobic surfaces featuring robust nanoscale (or hierarchical) roughness promote the growth of condensate drops in a suspended (or

Received: April 5, 2013

Revised: July 2, 2013

Published: July 3, 2013

partially suspended) Cassie state,<sup>18–21</sup> in sharp contrast to the aforementioned Wenzel condensate ubiquitous to superhydrophobic surfaces with microscale-only roughness. Nanoscale roughness minimizes the nucleation density of condensate relative to the density of surface features, which enables the majority of nucleating condensate to grow over the roughness in the energetically favorable Cassie state before coalescing with other drops.<sup>22–24</sup> When these superhydrophobic condensate drops were subcooled on a chilled nanostructured surface, they exhibited delayed condensation frosting compared to condensation on traditional surfaces.<sup>5,25–29</sup> As with deposited drops, subcooled superhydrophobic condensate can also be removed from the surface before freezing occurs, either by sliding off a vertically oriented condenser at millimetric length scales,<sup>28,30</sup> or by coalescence-induced jumping at micrometric length scales.<sup>29</sup> Even when subcooled condensate are continually removed from a nanostructured superhydrophobic surface, however, new condensate nucleates in its place, which will eventually freeze over due to a frost front that nucleates at surface defects and propagates across the entire surface through a chain reaction of interdrop ice bridges<sup>29</sup> or frost halos.<sup>31</sup> Freezing can also occur at the liquid–air interface of drops in the presence of chilled air flow.<sup>32</sup> Condensation frosting therefore seems inevitable even on nanostructured superhydrophobic surfaces, but can the Cassie state of the frosted condensate enhance the mobility of defrosted meltwater? Previously, it was observed that melted frost was able to slide off an oil-infused superhydrophobic surface at a 75° tilt angle;<sup>30</sup> to our knowledge, defrosting has not been characterized for nonlubricated nanostructured surfaces exhibiting superhydrophobic condensation in a suspended Cassie state.

Here, we report that when a sheet of frost on a nanostructured superhydrophobic surface is partially melted into a film of slush composed of water and ice, it is able to spontaneously dewet into mobile Cassie drops that slide off the surface at low tilt angles ( $\alpha < 15^\circ$ ). We will call this behavior *dynamic defrosting* because of the unusually low contact angle hysteresis of the melting frost, which simultaneously enables both its dewetting and mobilization from the surface. The contact line of the slush film spontaneously dewets (recedes) to form a large contact angle drop(s) corresponding to the system's equilibrium surface energy; this serves to dry the majority of the surface. The Cassie state of the melting slush promotes its rapid mobilization from the surface even at very low tilt angles, particularly after dewetting has occurred. Unlike the use of mechanical force to remove ice from a superhydrophobic surface,<sup>15,33</sup> the dynamic defrosting observed here did not affect the superhydrophobicity of the surface. Compared to thermal defrosting on nonsuperhydrophobic flat or microgrooved surfaces, where meltwater is imperfectly drained even at full 90° tilt angles,<sup>34</sup> a superhydrophobic surface can remove all meltwater at minimal tilt angles for any temperature above freezing. Nanostructured superhydrophobic surfaces are therefore ideal for systems in freezing and humid environments, as they not only delay the growth of frost<sup>29</sup> but also dynamically defrost with a minimum amount of time, heat, and gravitational energy.

## 2. MATERIALS AND METHODS

**2.1. Surface Fabrication.** The lithography-free fabrication of silicon nanopillars was achieved by dry etching into a thermally dewetted platinum mask. A 5 nm thick platinum film was deposited on 100 nm thermally grown SiO<sub>2</sub> on a <100> Si substrate using an

electron beam evaporator. The sample was heated in a Rapid Thermal Processor (RTP) furnace (Easy Tube 3000, First Nano, Ronkonkoma, NY) at full power for 8 s in a H<sub>2</sub> and Ar ambient. The measured maximum temperature within the process chamber was approximately 850 °C for 8 s. Two etching processes, that is, SiO<sub>2</sub> etch followed by Si etch, were carried out in an inductively coupled plasma ion etching system (Oxford Plasmalab 100, Oxford Instruments, U.K.). The etching process of the 100 nm SiO<sub>2</sub> was carried out in a mixture of O<sub>2</sub> and C<sub>4</sub>F<sub>8</sub> at flow rates of 2 and 45 sccm, respectively, at 15 °C, 7 mTorr, and 200 W RF for 65 s. The etching conditions for the Si layer were 5 sccm Ar, 25 sccm SF<sub>6</sub>, and 60 sccm C<sub>4</sub>F<sub>8</sub> flow rates at 10 mTorr and 30 W RF. An etching time of 9 min at 20 °C resulted in an etch depth of  $H = 1200 \pm 200$  nm. The pillar diameter was approximately  $D = 50 \pm 10$  nm, resulting in an aspect ratio of  $H/D \approx 25$ . The nanopillar array was disordered with an average pitch of  $P = 120 \pm 60$  nm to neighboring pillars. All uncertainties for the pillar measurements were taken to a 95% confidence interval for measurements of 25 nanopillars. This recipe has been previously reported,<sup>35</sup> but here we additionally coat the surface with chlorotrimethylsilane to render the nanostructured surface superhydrophobic. Samples of approximate dimensions 2 cm × 2 cm were cleaved for the experiments. To tune the aspect ratio of the nanopillars, three different platinum films of thickness 5, 10, and 15 nm were dewetted and etched for additional experiments (Figures S1–S3, Supporting Information).

To demonstrate dynamic defrosting on a practical material, superhydrophobic copper substrates known to promote suspended condensation<sup>29</sup> were used for select experiments. Copper alloy 101 was degreased for 10 min in acetone, immersed for 10 min in ethanol, and then rinsed with deionized water. The copper was then immersed for 10 min in 10 mM AgNO<sub>3</sub> to galvanically deposit silver micro- and nanoparticles. The roughened substrate was then immersed for 15 min in 2 mM of 1-hexadecanethiol in ethanol to render it superhydrophobic.

**2.2. Experimental Setup.** To grow a sheet of frost on the superhydrophobic surface, it was thermally bonded to a horizontally oriented Peltier stage (Deben MK3 Coolstage) and cooled down to –20 °C in a clean room where the ambient air was 21 °C with a humidity of  $32 \pm 5\%$ . The cooling rate of the Peltier stage was the same for each trial, with the stage cooling from 20 °C down to –20 °C in 85 s. Using a top-down microscope (Olympus BX51), it was observed that subcooled spherical condensate initially formed on the surface and exhibited robust jumping-drop behavior characteristic of nanostructured superhydrophobic surfaces (Figure S2, Supporting Information). Since the subcooled condensate were consistently able to jump off the surface before heterogeneous ice nucleation could occur, the frost did not originate on the superhydrophobic surface at all, but rather at defects located along the edges of the sample that proceeded to frost the entire surface via an interdrop frost wave.<sup>29</sup> This interdrop frost wave created the initial layer of Cassie frost suspended on top of the surface, which proceeded to grow dendrites upward toward the supersaturated ambient. A side-view camera was used to optically characterize the growing frost (Figure S4, Supporting Information); when the frost reached its desired thickness, the stage was heated up to either 0 or 1 °C (which required about 15 s) or to 25 °C (25 s) and the resulting defrosting behavior was observed.

Side-view imaging, contact angle measurements, and stage tilting were performed using a goniometer (Rame-Hart model 590) and its software package (DROPimage Advanced). Top-down imaging was captured with an additional camera (Motic Moticam 2500) suspended over the goniometer. The Peltier stage was cooled to –20 °C until a frost layer formed and grew to the desired thickness at the edge of the sample. The Peltier stage was then heated to initiate the dynamic defrosting. A defrosting temperature of 0 °C was used to characterize spontaneous dewetting, as this temperature minimized flow effects and thermal gradients. A defrosting temperature of 1 °C was used to measure the contact angle hysteresis of the dewetted meltwater. Finally, a defrosting temperature of 25 °C was used to demonstrate rapid defrosting.

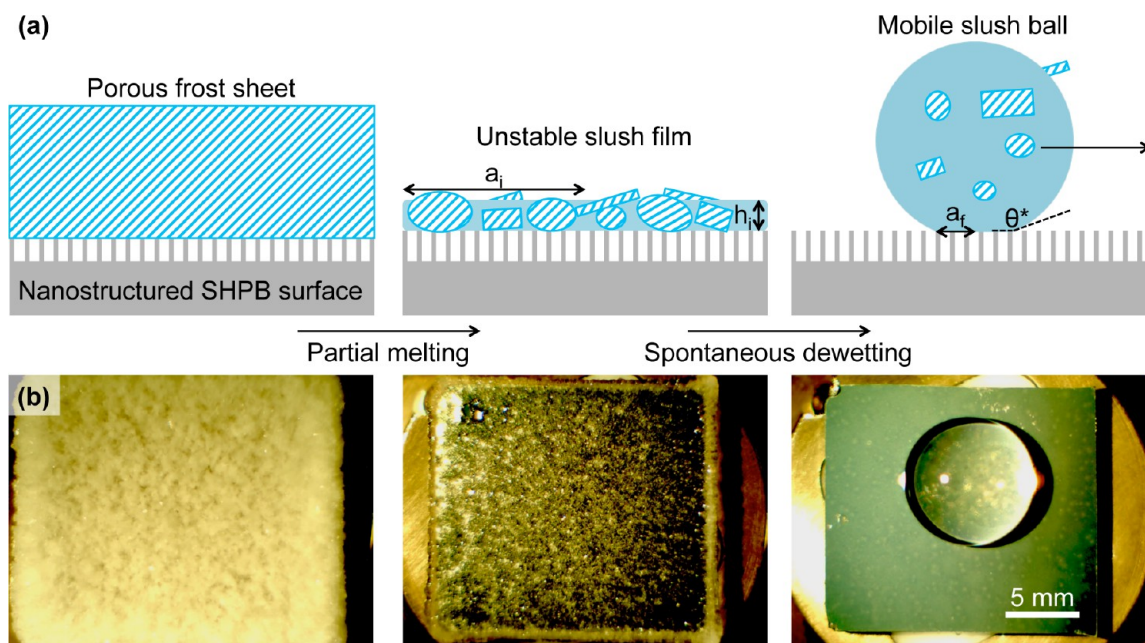


**Figure 1.** (a) Side-view schematic of the dynamic defrosting process. (b) Top-down imaging of dynamic defrosting. A porous frost sheet of thickness 2.0 mm melts into a film of slush exhibiting an initial height  $h_i = 0.6$  mm and contact radius  $a_i = 9.2$  mm that spontaneously dewets to a mobile drop with  $a_f = 3.4$  mm.

**2.3. Methods for Molecular Dynamics Simulation.** A proton disordered configuration of ice  $I_h$  was generated for a system containing 73 600 molecules of water using the algorithm of Buch et al.<sup>36</sup> The algorithm of Buch et al. allows generating ice configurations that satisfy the Bernal-Fowler rules. We added an additional condition: the block of ice should have a net dipole moment as low as possible. Although the algorithm of Buch et al. usually finds for small systems (i.e., of the order of 1000 molecules) a proton disordered configuration with low dipole moment in just a few minutes, the algorithm required more than two days of CPU time to find such a configuration in our system. The dimensions of the final orthorhombic block of ice were (approximately)  $180 \text{ \AA} \times 180 \text{ \AA} \times 73 \text{ \AA}$ . The dipole moment of the final configuration was about 500 D, which can be regarded as a small polarization. In fact, this is just  $1/360$  times the polarization that could adopt a complete ferroelectric ice (for the SPC/E model of water). This initial ice configuration was subsequently reduced in the  $z$ -direction so as to produce dewetting dynamics where rim formation was easier to observe. This resulted in an ice slab with dimensions  $188 \text{ \AA} \times 188 \text{ \AA} \times 48 \text{ \AA}$  and 5,0345 water molecules; this is the slab that we deposited on top of the pillared graphite. The pillared graphite in our simulations is composed of a single graphene layer. The atoms in the pillared substrate atoms are kept immobile throughout the simulation, whereas the water molecules are kept at a constant temperature by employing the Nose-Hoover thermostat. The total number of atoms in the system, that is, water plus carbon atoms, is 339 195. The lateral dimension  $L$ , that is, the extent from the left to the right edge of ice, was used to measure the dynamical changes caused by dewetting. Using  $L$  allowed us to exclude the center of mass translational motion. The location of the edges was determined as the point at which the density becomes smaller than 85% of the density in the center of the slab.

Molecular dynamics simulations were performed using the LAMMPS package.<sup>37</sup> In order to achieve acceptable run times, simulations were performed using GPU acceleration<sup>38,39</sup> on Cray XK7 nodes. The long-range electrostatics were calculated using particle-particle particle-mesh (P3M). Because P3M is implicitly periodic, artificial periodicity in the  $z$  dimension was removed by extending the P3M mesh with empty volume in the  $z$  dimension and removing dipole interactions between the  $x$ - $y$  slabs.<sup>40</sup> In order to mitigate the performance impact from this approach, fast Fourier transforms for the P3M Poisson solve were performed in single precision and the short-

range direct summation performed on the GPU was extended to a cutoff of  $16 \text{ \AA}$  to decrease the size of the mesh required for accurate calculations.<sup>41</sup> Dynamic load balancing was used to address the nonuniform atom density for the simulations. The bond angles and bond length within each water molecule were constrained using the SHAKE algorithm. The simulation time step was set to be 1.5 fs. We ran simulations at  $T = 245 \text{ K}$  for 5–10 ns, which required approximately 18–36 h on 16 XK7 computer nodes. To ascertain that the results were statistically consistent, multiple independent runs were performed from different random seeds for the initial velocity profile of the water molecules.

### 3. RESULTS

Figure 1 depicts the dynamic defrosting of the nanostructured superhydrophobic surface that occurred when the sample was heated from  $-20$  to  $0 \text{ }^\circ\text{C}$ . Figure 1a is a schematic that illustrates the melting of the initial frost sheet into an unstable slush film, which proceeds to dewet from the superhydrophobic surface into a more energetically desirable shape. This is experimentally observed in Figure 1b, where a top-down camera captures the spontaneous dewetting of the melting frost sheet into a Cassie drop. It is remarkable that this spontaneous dewetting occurs even when the substrate is held at  $0 \text{ }^\circ\text{C}$  and the meltwater's contact area remains partially frozen. Although the humidity was held constant at  $32 \pm 5\%$  for the majority of experiments, dynamic defrosting was observed for the full range of humidities possible within the current experimental setup, which spanned from 25% to 48% (cf. Figure 4). While it has been previously observed that *deposited* Cassie drops frozen on a superhydrophobic surface can be restored to their original spherical shape by melting the ice back into liquid,<sup>8,11</sup> this is the first report of transforming an initially flattened sheet of frost into a dewetted, highly mobile Cassie drop upon partial melting. A very recent report noted that shifting ice could push neighboring drops off a horizontal superhydrophobic surface;<sup>42</sup> here, we utilize slow melting at  $0 \text{ }^\circ\text{C}$  to fully characterize defrosted meltwater without resorting to external forcing from ice.

While the suspended Cassie state of the frost sheet cannot be directly observed here, it may be strongly inferred from three related observations. First, the subcooled condensate initially formed on the surface in a suspended, jumping-drop state (Figure S2, see the Supporting Information), so it follows that the resulting interdrop frost front<sup>29</sup> would be similarly elevated. Second, upon defrosting the frost sheet into a film of slush, its contact line was able to spontaneously dewet (recede) from the surface, an unlikely behavior for liquid in the impaled Wenzel state.<sup>17</sup> Finally, the ability of the dewetted slush ball to slide off the surface at low tilt angles ( $\alpha < 15^\circ$ ) is solely possible in a Cassie state.<sup>4</sup> It should be emphasized that the Cassie state of condensate forming on superhydrophobic nanostructures is not perfect; typically, a small portion of each drop's contact area is partially impaled in the roughness.<sup>22–24</sup> Therefore, the resulting frost is also likely to exhibit an imperfect Cassie state, as evidenced here by localized nanopillars bundling together after a frost/defrost cycle (Figure 2). Since partial wetting states are often reversible with energy input,<sup>17</sup> it is possible that the large amount of free energy harvested during dewetting could facilitate a dewetting transition to a fuller Cassie state for the meltwater. Regardless, the Cassie state of the frost is sufficient to enable the spontaneous dewetting and rapid mobilization of the resulting meltwater, which is not possible for aggressive Wenzel states. In the future, the specific wetting state of the initial frost sheet could be experimentally characterized by employing cryogenic focused ion beam (FIB) milling in conjunction with SEM imaging.<sup>43</sup>

The Cassie state of the frost is a direct result of the Cassie state of the initial subcooled condensate, which is the most robust for high-aspect ratio nanoroughness (Figures S2, S3). The dynamic defrosting phenomenon is therefore expected to occur for any nanostructured (or hierarchical) superhydrophobic surface that promotes suspended, jumping-drop type condensation. Two recent reports have characterized the key design parameters for nanostructured roughness to promote suspended condensation.<sup>23,24</sup> Therefore, this current report focuses on characterizing the dynamic defrosting phenomenon itself rather than any design parameters for the surface roughness.

**3.1. Mechanical Durability.** The physical and chemical durability of a superhydrophobic surface undergoing numerous icing/deicing cycles is of great practical importance. When a sheet of ice<sup>15,33</sup> or a frozen drop<sup>44</sup> is mechanically removed from a superhydrophobic surface, the surface roughness partially breaks off as well, even if the ice is in the minimally invasive Cassie state.<sup>15,33,44</sup> This results in the wettability, contact angle hysteresis, and ice adhesion strength of the surface gradually increasing after each icing/deicing cycle.<sup>15,33</sup> It remains unknown whether a noninvasive thermal defrosting would similarly diminish the robustness of a superhydrophobic surface.

In Figure 2a, the advancing and receding contact angles of pendant drops were measured at room temperature with a contact angle goniometer between ten frost/defrost cycles on the nanostructured superhydrophobic surface. Three trials were performed between each frost/defrost cycle, and the uncertainty was taken to a 95% confidence interval for all 33 trials. The surface's contact angle hysteresis was consistently negligible, with advancing and receding contact angles of  $\theta_A = 168 \pm 3^\circ$  and  $\theta_R = 166 \pm 3^\circ$  throughout all 10 frost/defrost cycles. This indicates that the dynamic defrosting of Cassie ice from a nanostructured superhydrophobic surface does not

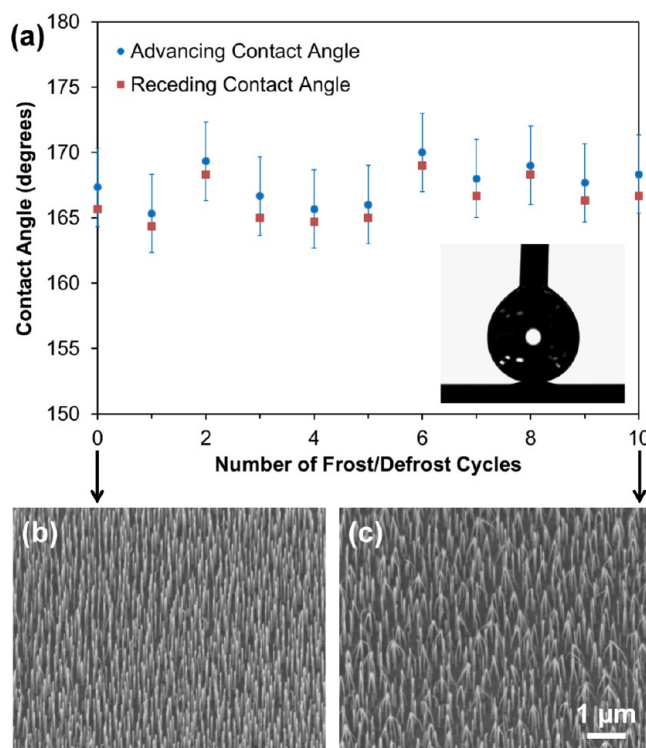


**Figure 2.** (a) The small contact angle hysteresis of drops deposited on the nanostructured superhydrophobic surface is not affected by 10 frost/defrost cycles. For visual clarity, the uncertainty of  $\theta_R$  is omitted. (b, c) SEM images of the silicon nanopillars (b) before and (c) after the frost/defrost cycles.

cause any appreciable damage to the surface roughness. Figure 2b, c shows the scanning electron microscopy (SEM) images of the nanopillars before and after the ten frost/defrost cycles. It can be seen that the nanopillars tended to bundle together after frost/defrost cycles due to capillarity effects,<sup>45</sup> but are still vertically aligned and otherwise unharmed. Based on the consistent apparent contact angle of droplets throughout all frost/defrost cycles, the surface's effective solid fraction is not expected to have changed appreciably. The possibility of diminished superhydrophobicity after hundreds or thousands of frost/defrost cycles cannot currently be ruled out; however, recent reports of durable porous nanostructures on aluminum<sup>46</sup> and copper<sup>47</sup> exhibiting similar jumping-drop condensation could enable more practical implementations of the dynamic defrosting phenomenon observed here.

**3.2. Energetics of Dewetting.** While the initial sheet of porous frost is completely frozen, as it melts into a film of slush, the partial presence of water begins to pull the slush upward toward the shape corresponding to its equilibrium surface energy. The Gibb's free energy of the initial slush film can be approximated as<sup>4</sup>

$$E_i = (\pi a_i^2)(2 - \phi(1 + \cos \theta_Y))\gamma + \frac{1}{2}\rho g V h_i \quad (1)$$

where  $\phi$  and  $\theta_Y$  are the solid fraction and Young's contact angle of the slush film with the surface,  $\gamma$  and  $\rho$  are the surface tension and density of water,  $g$  is gravity, and  $a_i$ ,  $h_i$ , and  $V$  are the contact radius, height, and volume of the initial slush film, respectively. The initial contact radius of the slush film ( $a_i$ ) is approximately equal to the radius of the substrate, the initial height ( $h_i$ ) corresponds to the minimum thickness attained by

the melting slush film before dewetting begins, and its volume may be estimated by  $V \approx \pi a_i^2 h_i$ . Here, it was observed that  $h_i$  was approximately 1/4 the thickness of the original frost sheet. Using the Young's and apparent contact angles of  $\theta_Y \approx 100^\circ$  and  $\theta^* \approx 167^\circ$  (Figure 2a), an effective solid fraction of approximately  $\phi \approx 0.03$  can be extrapolated from the Cassie equation:<sup>4</sup>

$$\phi = \frac{\cos \theta^* + 1}{\cos \theta_Y + 1} \quad (2)$$

Once the slush puddle has finished dewetting into a single spherical-cap drop, the free energy of the final system is given by

$$E_{f,d} = (\pi a_{f,d}^2) \left( \frac{2(1 - \cos \theta^*)}{\sin^2 \theta^*} + 1 - \phi(1 + \cos \theta_Y) \right) \gamma \quad (3)$$

where  $a_{f,d}$  is the contact radius of the final drop which can be deduced from the geometric relation:

$$a_{f,d} = \sin \theta^* \left( \frac{3V}{\pi(2 + \cos \theta^*)(1 - \cos \theta^*)^2} \right)^{1/3} \quad (4)$$

If the size of the dewetted slush exceeds the capillary length,  $\kappa^{-1} \sim (\gamma/\rho g)^{1/2}$ , gravity will flatten the top of the drop to remove its spherical-cap shape (for water at 0 °C,  $\kappa^{-1} \approx 3$  mm). These large, flattened drops are called puddles.<sup>4</sup> Therefore, when the volume of the slush is sufficiently large ( $V > 10 \mu\text{L}$ ), as will be the case for most practical systems, it will remain at least partially flattened upon dewetting as opposed to exhibiting a spherical-cap profile. This does not negate the dewetting process as long as the thickness of the initial slush film was not already at equilibrium. The final free energy of a dewetted puddle is given by

$$E_{f,p} = (\pi a_{f,p}^2)(2 - \phi(1 + \cos \theta_Y))\gamma + \frac{1}{2}\rho g V h_{f,p} \quad (5)$$

where the final height of the puddle corresponds to its equilibrium value,  $h_{f,p} = h_e = 2\kappa^{-1} \sin(\theta^*/2)$ ,<sup>4</sup> and the final contact radius is given by  $a_{f,p} \approx (V/\pi h_{f,p})^{1/2}$ . For simplicity, this analysis neglects the complex shapes exhibited by drops of intermediate sizes.<sup>49</sup> Putting everything together, it is energetically favorable for a slush puddle to dewet from the surface when

$$\frac{E_i}{E_f} = E^* > 1 \quad (6)$$

The value of  $E^*$  can be calculated by approximating the dewetting slush film as pure water at 0 °C ( $\gamma = 75.6$  mN/m and  $\rho = 1000$  kg/m<sup>3</sup>). This simplification is supported by a molecular dynamics simulation indicating that the slush film must melt to at least 90% water before appreciable dewetting occurs (see section 4). When holding the initial contact radius ( $a_i$ ) of the slush film constant, analogous to fixing the area of the frosted substrate, the energy harvested by dewetting ( $E^*$ ) increases with decreasing film thickness ( $h_i$ ). For example,  $E^* = 28$  when a slush film of initial height  $h_i = 0.1$  mm dewets to a puddle, compared to  $E^* = 2.8$  for  $h_i = 1$  mm. This is because an increasing amount of energy is required to flatten a slush film below its equilibrium thickness. Here,  $h_e \approx 5$  mm, which was experimentally observed with the dewetted puddle depicted in section 3.4 (Figure 4). Therefore, the dynamic defrosting

phenomenon may be considered analogous to the compression and release of a spring, where thinner frost sheets correspond to a greater spring compression, and melting the frost into slush corresponds to releasing the compressed spring. When  $h_i$  is held constant,  $E^*$  increases with  $a_i$  when dewetting to small spherical-cap drops, while remaining independent of  $a_i$  when dewetting to puddles. Most importantly, spontaneous dewetting is energetically favorable ( $E^* > 1$ ) for surface areas of any size, provided that  $h_i < h_e$ . Here, the dependence of the dewetting time-scale on  $E^*$  could not be characterized due to the slow melting time of the frost; future studies could utilize high-temperature defrosting to better isolate the dewetting kinetics.

**3.3. Continuity of Dewetting.** Depending on the thickness of the initial frost sheet, the melting slush film could either dewet into one large drop or into multiple drops. This was experimentally characterized in Figure 3, where the

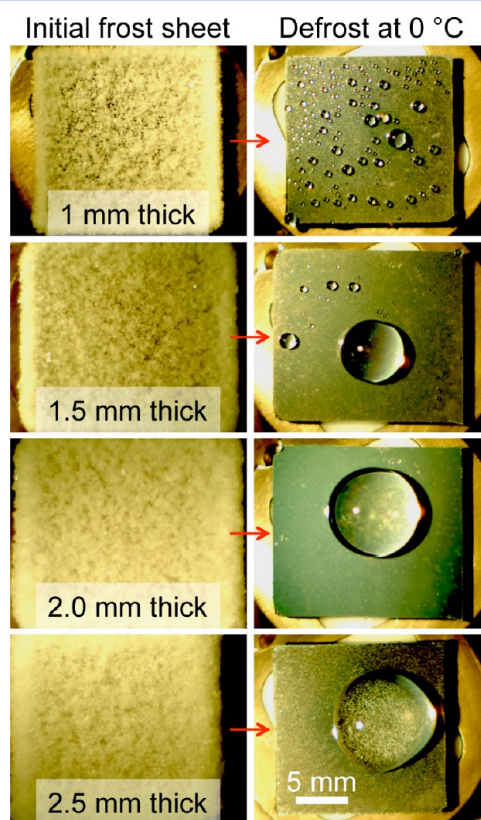


**Figure 3.** Thin frost sheets of thickness 1.0 mm and 1.5 mm defrosted into multiple drops (standard deviation of  $226 \pm 148$  and  $15 \pm 8$  drops, respectively, over three trials). For frost sheets exhibiting a thickness of 2 mm or greater, the defrosting slush consistently dewetted as one continuous drop/puddle. Movies M1–M4 are available in the Supporting Information.

dewetting slush film was only continuous for initial frost layers of thickness 2 mm or greater. It has been previously reported that liquid coatings can destabilize upon dewetting due to hole nucleation or spinodal dewetting;<sup>50</sup> however, these types of instabilities are inherent to ultrathin films as opposed to the macroscopically thick films used here. Instead, we suggest that the primary mechanism of liquid breakup is the poor interconnectivity of the thin frost sheet prior to melting. This was evidenced by the exposed dry spots and isolated frost balls

visible on the superhydrophobic surface for frost layers thinner than 2 mm.

While hydrophilic substrates typically exhibit continuous films of frost early on in their growth,<sup>27</sup> the initial frosting of dropwise condensate on hydrophobic surfaces is less straightforward. When an interdrop frost front spreads across subcooled spherical condensate on a jumping-drop superhydrophobic surface, only about 1/3 of the drops are successfully frozen into frost, while the other 2/3 of drops completely evaporate.<sup>29</sup> This minimizes the surface coverage and connectivity of the frost on the substrate, and therefore a critical amount of upward dendrite growth toward the supersaturated ambient is subsequently required to adequately interconnect the entire frost sheet. For thin frost sheets, multiple drops can form upon dewetting for two different reasons: in some cases, frozen drops might be completely isolated without any surviving bridges to neighboring drops, while in other cases an ice bridge(s) may initially exist between frozen drops that destabilizes upon melting when the length-to-width aspect ratio of the bridging liquid filament exceeds a critical value.<sup>51</sup>

The large surface tension and low viscosity of water suggest a potential analog to the dewetting of liquid metal films,<sup>52</sup> where Rayleigh–Plateau flow instabilities can additionally break up thin strands of dewetting liquid.<sup>53</sup> However, a slow defrosting temperature of 0 °C was deliberately used in Figure 3 to minimize flow effects during melting and dewetting. The 0 °C temperature was also chosen to minimize instabilities caused by temperature gradients, as the area of the Peltier stage was smaller than the area of the bonded substrate. It would seem that dynamic defrosting is optimized when the frost sheet is thick enough to be continuous upon melting (Figure 3), but still thin enough to harvest a significant amount of free energy via dewetting (eq 6).

**3.4. Facile Shedding of Dewetted Melt-Water.** The hysteresis of the dewetted meltwater was measured by tilting the goniometer stage in 1° increments until the drop slid off the surface. An initial frost sheet of thickness 1.5 mm was used, such that upon heating to 0 °C the largest dewetted drop was small enough to be captured in the side-view camera's field-of-view to calculate its volume. After a defrosted drop was finished dewetting, the substrate temperature was increased from 0 to 1 °C to melt the remaining ice in the drop for better repeatability (the hysteresis of meltwater at 0 °C varied widely). The tilt angle required to shed dewetted meltwater of volume  $V = 79 \pm 10 \mu\text{L}$  was  $\alpha = 13 \pm 1^\circ$ , where the uncertainty corresponds to a 95% confidence interval over three trials. This gravitational energy can be related to the contact angle hysteresis by  $\rho V g \sin \alpha = \pi a \gamma (\cos \theta_R - \cos \theta_A)$ .<sup>54</sup> This yields  $\cos \theta_R - \cos \theta_A = 0.268 \pm 0.005$ , larger than the hysteresis of the deposited drops at room temperature (Figure 2) but comparable to previous reports of Cassie drops deposited on dry superhydrophobic substrates exhibiting small solid fractions  $\phi < 0.1$ .<sup>55</sup> While still very low compared to Wenzel drops, there are two reasons why the hysteresis of the meltwater is larger than with the deposited drops: the previously discussed imperfect Cassie state of the frost/meltwater, and the presence of condensate around the meltwater's contact line.

The lower limit in dewetted puddle volume ( $V_c \approx \pi a_c^2 h_c$ ) required for successful mobilization at a given tilt angle may be estimated by

$$V_c \approx \frac{\pi}{h_c} \left( \frac{\gamma (\cos \theta_R - \cos \theta_A)}{\rho g \sin \alpha} \right)^2 \quad (7)$$

For example, here a tilt angle of  $\alpha = 15^\circ$  is capable of shedding meltwater larger than  $V_c \approx 36 \mu\text{L}$ . When  $\alpha = 75^\circ$ , used for the previously reported defrosting of lubricated nanostructures,<sup>30</sup> the critical volume reduces by an order of magnitude to  $V_c \approx 3 \mu\text{L}$ . While eq 7 begins to break down at such small volumes, assuming a spherical-cap shape yields the same approximate volume. Equation 7 highlights the advantage of defrosting mature, well-connected frost sheets into large-volume puddles (cf. Figure 3), which slide off easier compared to defrosting premature frost sheets into disconnected small-volume drops.

The low contact angle hysteresis of the dewetted meltwater is remarkable given the low surface temperature of 1 °C, where liquid condensate visibly formed on the substrate and surrounded the drop's contact line (Figure 4). It has been

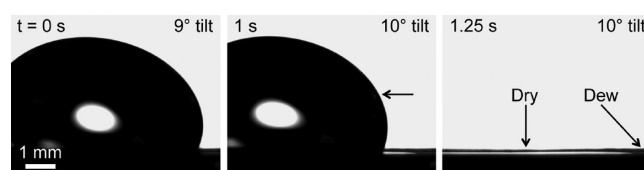


**Figure 4.** A sheet of frost 2.5 mm thick was defrosted at 1 °C on a horizontally oriented superhydrophobic surface. A higher humidity of 45% was employed here to emphasize the mobility of defrosted drops even in the extreme presence of condensate. The meltwater was able to slide off the surface at a low critical tilt angle of  $\alpha = 10^\circ$ . Since the 1 °C surface was well beneath the dew point of 9 °C, the high mobility of the defrosted drop is particularly impressive given that it had to slide through a significant amount of dew forming around it on the surface (as indicated by the dry patch left behind in the final frame). See Movie M5 in the Supporting Information.

previously reported that the impaled condensate that forms on superhydrophobic surfaces cooled beneath the dew point inhibits the mobility of drops.<sup>56,57</sup> The suspended Cassie state of the jumping-drop condensate observed here seems to mitigate this problem. These results demonstrate that the facile shedding of melting frost and ice from nanostructured superhydrophobic surfaces is possible even at temperatures well below the dew point, in sharp contrast to traditional surfaces where the defrosting temperature typically exceeds 25 °C.<sup>2</sup>

In additional experiments, the substrate was already tilted at  $\alpha = 10^\circ$  before defrosting began, in which case the dewetting slush drops were able to mobilize from the surface while still containing significant amounts of ice (Figures 5, 6). To verify that dynamic defrosting should occur for any surface exhibiting suspended jumping-drop condensate, a superhydrophobic copper substrate known for robust jumping-drop behavior<sup>29</sup> was also observed to exhibit dynamic defrosting (Figure 5). The time scale for the frost to (partially) melt, dewet, and mobilize from the tilted surface depended on the thickness of the frost and the defrosting temperature, but for frost sheets of thickness  $\sim 1$  mm was on the order of  $t \sim 10$  s at 25 °C (Figure 5) and  $t \sim 1$  min at 0 °C (Figure 6).

#### 4. MOLECULAR DYNAMICS SIMULATION

To gain qualitative insight into the dewetting process, we have performed molecular dynamics (MD) simulations on a substrate that resembles the structure used in the experiment,

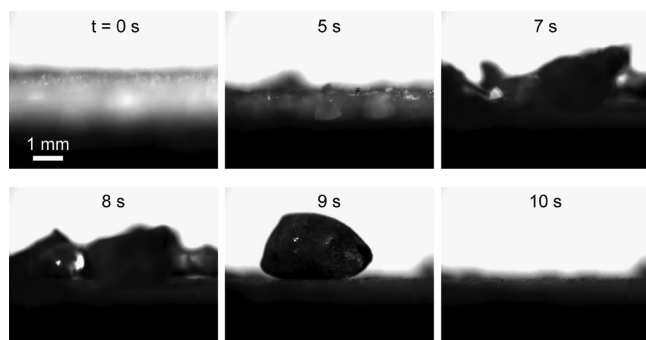


**Figure 5.** Side-view imaging of dynamic defrosting on a superhydrophobic copper substrate. A frost sheet approximately 1 mm thick was defrosted at 25 °C. Utilizing a constant tilt angle of  $\alpha = 10^\circ$ , the melting frost was able to dewet and mobilize from the surface within 10 s. Time zero corresponds to the heated surface reaching 0 °C and the meltwater was completely mobilized by the time the surface reached 25 °C about 10 s later. The hierarchical copper substrate, used in this figure only instead of the silicon sample, demonstrates that any superhydrophobic surface exhibiting robust jumping-drop condensation should also exhibit the dynamic defrosting phenomenon due to the Cassie state of the resulting frost. See Movie M6 in the Supporting Information.

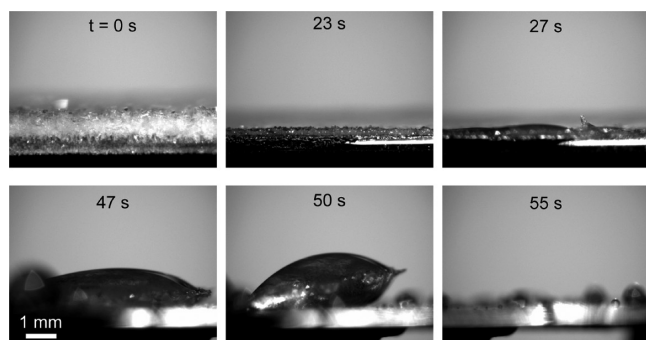


**Figure 6.** At time zero, a sheet of frost 1 mm thick was defrosted at a temperature of 0 °C and a constant tilt angle of  $\alpha = 10^\circ$ . The partially melted slush was able to dewet and slide off the surface in under 1 min even though it still contained large pieces of ice. This experiment also illustrates the disadvantage of thin, discontinuous frost sheets: the slush broke up into additional, smaller droplets that were unable to mobilize along with the larger slush drop. See Movie M7 in the Supporting Information.

that is, pillared graphite. The interaction between water molecules was described with the SPC/E model,<sup>58</sup> which has been found to reproduce well many of the properties of water. For ice in the  $I_h$  structure, the SPC/E model gives a melting point of 215 K. The interaction between water (its O atoms only) and graphite was described using a 12-6 Lennard–Jones potential, where  $\epsilon_{C-O} = 0.03$  kcal/mol and  $\sigma = 3.0$  Å. A potential with the same  $\epsilon_{C-O}$  was used before to describe water on graphite and was found to yield a contact angle greater than  $140^\circ$ .<sup>59</sup> It should be noted that the results produced with these potentials can only be compared to the experiment in a qualitative manner. Quantitative comparisons could be obtained if one were to use other types of simulation techniques, that is, ab initio techniques, but the size of the system simulated here is prohibitively large for ab initio calculations. The water molecules were initialized in a proton-disordered hexagonal  $I_h$  structure. From this structure, a slab was extracted and placed on top of the substrate. The slab was

then heated rapidly to 245 K and kept at this temperature throughout the simulation time. It should be noted that 245 K is well above the melting temperature, 215 K, of ice  $I_h$  as simulated with SPC/E.<sup>60</sup>

The snapshots in Figure 7a show that the ice slab dewets to the shape of a spherical drop during melting. There is

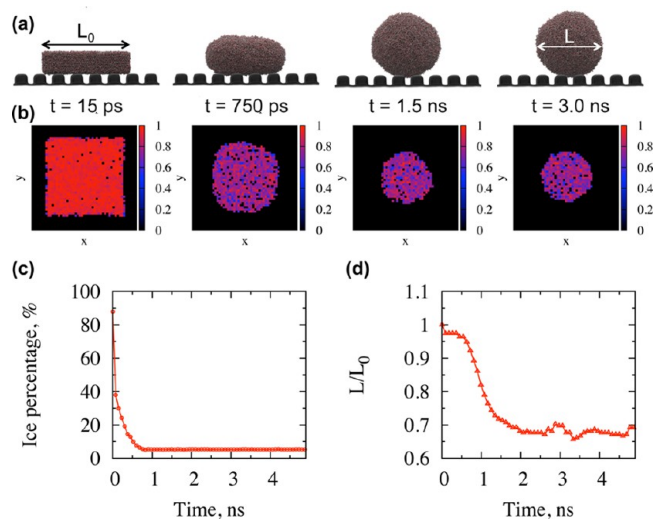


**Figure 7.** (a) Molecular dynamics simulation of a melting ice sheet dewetting on a superhydrophobic surface (see movie M8 in the Supporting Information). (b) Corresponding top-down characterization of the tetrahedral index ( $q_i$ ) during melting, where  $q_i \geq 0.91$  signifies icelike molecules. (c,d) The ice needs to melt to approximately 90% water for appreciable dewetting to occur.

practically no dewetting up to about 0.5 ns; then water retraction takes place in a very sudden manner and continues until about 1.5 ns, where it approaches equilibrium. To understand this behavior, we have calculated the tetrahedral index  $q_i$ , which can be used to classify the molecules as being in an icelike or liquidlike environment (Figure 7b).<sup>61</sup> For  $q_i \geq 0.91$ , the molecules are considered to be in an icelike environment. Figure 7c shows the time evolution of the percentage of oxygen atoms for which  $q_i \geq 0.91$ . Interestingly, at 0.5 ns, that is, at the time where the lateral retraction starts (Figure 7d), approximately only 10% of the molecules can be considered to be in an ice-like environment. Thus, it seems that for appreciable dewetting to occur, the ice slab must be approximately 90% melted. It remains to be seen whether this percentage depends on the size and shape of the ice slab and is an issue that we are currently investigating.

## 5. CONCLUSION

In conclusion, we have demonstrated that when a sheet of frost is partially melted into a mixture of water and ice on a nanostructured superhydrophobic surface, it is able to spontaneously dewet and mobilize from the surface at low tilt angles approaching zero. This dynamic defrosting is energetically driven by the water in the slush puddle dewetting to minimize its surface energy and is physically enabled by the mobile Cassie state of the slush. Nanostructured superhydrophobic surfaces seem uniquely capable of promoting frost growth in a Cassie state that can be effectively shed at any temperature above freezing.

## ■ ASSOCIATED CONTENT

### ■ Supporting Information

Additional figures depicting condensation, frosting, and defrosting on superhydrophobic nanostructures with varying geometric parameters (Figures S1–S4) and 14 movies representative of Figures 3–7 and Figures S2, S3. This material is available free of charge via the Internet at <http://pubs.acs.org>.

## ■ AUTHOR INFORMATION

### Corresponding Author

\*E-mail: [colliercp@ornl.gov](mailto:colliercp@ornl.gov).

### Notes

The authors declare no competing financial interest.

## ■ ACKNOWLEDGMENTS

The authors acknowledge W. Michael Brown for technical assistance regarding the simulation setup and Jason D. Fowlkes and Scott T. Retterer for helpful discussions.

## ■ REFERENCES

- (1) Wang, W.; Xiao, J.; Guo, Q. C.; Lu, W. P.; Feng, Y. C. Field Test Investigation of the Characteristics for the Air Source Heat Pump under Two Typical Mal-Defrost Phenomena. *Appl. Energy* **2011**, *88*, 4470–4480.
- (2) Wang, W.; Xiao, J.; Feng, Y.; Guo, W.; Wang, L. Characteristics of an Air Source Heat Pump with Novel Photoelectric Sensors during Periodic Frost-Defrost Cycles. *Appl. Therm. Eng.* **2013**, *50*, 177–186.
- (3) Meuler, A. J.; McKinley, G. H.; Cohen, R. E. Exploiting Topographical Texture To Impart Icephobicity. *ACS Nano* **2010**, *4*, 7048–7052.
- (4) Quere, D. Non-Sticking Drops. *Rep. Prog. Phys.* **2005**, *68*, 2495–2532.
- (5) Wang, H.; Tang, L.; Wu, X.; Dai, W.; Qiu, Y. Fabrication and Anti-Frosting Performance of Super Hydrophobic Coating Based on Modified Nano-Sized Calcium Carbonate and Ordinary Polyacrylate. *Appl. Surf. Sci.* **2007**, *253*, 8818–8824.
- (6) Tourkine, P.; Merrer, M. L.; Quere, D. Delayed Freezing on Water Repellent Materials. *Langmuir* **2009**, *25*, 7214–7216.
- (7) Cao, L.; Jones, A. K.; Sikka, V. K.; Wu, J.; Gao, D. Anti-Icing Superhydrophobic Coatings. *Langmuir* **2009**, *25*, 12444–12448.
- (8) Mishchenko, L.; Hatton, B.; Bahadur, V.; Taylor, J. A.; Krupenkin, T.; Aizenberg, J. Design of Ice-free Nanostructured Surfaces Based on Repulsion of Impacting Water Droplets. *ACS Nano* **2010**, *4*, 7699–7707.
- (9) Jung, S.; Dorrestijn, M.; Raps, D.; Das, A.; Megaridis, C. M.; Poulikakos, D. Are Superhydrophobic Surfaces Best for Icephobicity? *Langmuir* **2011**, *27*, 3059–3066.
- (10) Alizadeh, A.; Yamada, M.; Li, R.; Shang, W.; Otta, S.; Zhong, S.; Ge, L.; Dhinojwala, A.; Conway, K. R.; Bahadur, V.; Vinciguerra, A. J.; Stephens, B.; Blohm, M. L. Dynamics of Ice Nucleation on Water Repellent Surfaces. *Langmuir* **2012**, *28*, 3180–3186.
- (11) Guo, P.; Zheng, Y.; Wen, M.; Song, C.; Lin, Y.; Jiang, L. Icephobic/Anti-Icing Properties of Micro/Nanostructured Surfaces. *Adv. Mater.* **2012**, *24*, 2642–2648.
- (12) Lafuma, A.; Quere, D. Superhydrophobic States. *Nat. Mater.* **2003**, *2*, 457–460.
- (13) Wier, K. A.; McCarthy, T. J. Condensation on Ultrahydrophobic Surfaces and Its Effect on Droplet Mobility: Ultrahydrophobic Surfaces Are Not Always Water Repellent. *Langmuir* **2006**, *22*, 2433–2436.
- (14) Varanasi, K. K.; Deng, T.; Smith, J. D.; Hsu, M.; Bhate, N. Frost Formation and Ice Adhesion on Superhydrophobic Surfaces. *Appl. Phys. Lett.* **2010**, *97*, 234102.
- (15) Kulinich, S. A.; Farhadi, S.; Nose, K.; Du, X. W. Superhydrophobic Surfaces: Are They Really Ice-Repellent? *Langmuir* **2011**, *27*, 25–29.
- (16) Chen, J.; Liu, J.; He, M.; Li, K.; Cui, D.; Zhang, Q.; Zeng, X.; Zhang, Y.; Wang, J.; Song, Y. Superhydrophobic Surfaces Cannot Reduce Ice Adhesion. *Appl. Phys. Lett.* **2012**, *101*, 111603.
- (17) Boreyko, J. B.; Baker, C. H.; Poley, C. R.; Chen, C. H. Wetting and Dewetting Transitions on Hierarchical Superhydrophobic Surfaces. *Langmuir* **2011**, *27*, 7502–7509.
- (18) Lau, K. K. S.; Bico, J.; Teo, K. B. K.; Chhowalla, M.; Amaratunga, G. A. J.; Milne, W. I.; McKinley, G. H.; Gleason, K. K. Superhydrophobic Carbon Nanotube Forests. *Nano Lett.* **2003**, *3*, 1701–1705.
- (19) Chen, C. H.; Cai, Q.; Tsai, C.; Chen, C. L.; Xiong, G.; Yu, Y.; Ren, Z. Dropwise Condensation on Superhydrophobic Surfaces with Two-Tier Roughness. *Appl. Phys. Lett.* **2007**, *90*, 173108.
- (20) Boreyko, J. B.; Chen, C. H. Self-Propelled Dropwise Condensate on Superhydrophobic Surfaces. *Phys. Rev. Lett.* **2009**, *103*, 184501.
- (21) Miljkovic, N.; Enright, R.; Wang, E. N. Effect of Droplet Morphology on Growth Dynamics and Heat Transfer during Condensation on Superhydrophobic Nanostructured Surfaces. *ACS Nano* **2012**, *6*, 1776–1785.
- (22) Rykaczewski, K. Microdroplet Growth Mechanism during Water Condensation on Superhydrophobic Surfaces. *Langmuir* **2012**, *28*, 7720–7729.
- (23) Rykaczewski, K. How Nanorough is Rough Enough to Make a Surface Superhydrophobic During Water Condensation? *Soft Matter* **2012**, *8*, 8786–8794.
- (24) Enright, R.; Miljkovic, N.; Al-Obeidi, A.; Thompson, C. V.; Wang, E. N. Condensation on Superhydrophobic Surfaces: The Role of Local Energy Barriers and Structure Length Scale. *Langmuir* **2012**, *28*, 14424–14432.
- (25) He, M.; Wang, J.; Li, H.; Jin, X.; Wang, J.; Liu, B.; Song, Y. Super-Hydrophobic Film Retards Frost Formation. *Soft Matter* **2010**, *6*, 2396–2399.
- (26) He, M.; Wang, J.; Li, H.; Song, Y. Super-Hydrophobic Surfaces to Condensed Micro-Droplets at Temperatures Below the Freezing Point Retard Ice/Frost Formation. *Soft Matter* **2011**, *7*, 3993–4000.
- (27) Zhang, Q.; He, M.; Zeng, X.; Li, K.; Cui, D.; Chen, J.; Wang, J.; Song, Y.; Jiang, L. Condensation Mode Determines the Freezing of Condensed Water on Solid Surfaces. *Soft Matter* **2012**, *8*, 8285–8288.
- (28) Zhang, Y.; Yu, X.; Wu, H.; Wu, J. Facile Fabrication of Superhydrophobic Nanostructures on Aluminum Foils with Controlled-Condensation and Delayed-Icing Effects. *Appl. Surf. Sci.* **2012**, *258*, 8253–8257.
- (29) Boreyko, J. B.; Collier, C. P. Delayed Frost Growth on Jumping-Drop Superhydrophobic Surfaces. *ACS Nano* **2013**, *7*, 1618–1627.
- (30) Kim, P.; Wong, T. S.; Alvarenga, J.; Kreder, M. J.; Adorno-Martinez, W. E.; Aizenberg, J. Liquid-Infused Nanostructured Surfaces with Extreme Anti-Ice and Anti-Frost Performance. *ACS Nano* **2012**, *6*, 6569–6577.
- (31) Jung, S.; Tiwari, M. K.; Poulikakos, D. Frost Halos from Supercooled Water Droplets. *Proc. Natl. Acad. Sci. U.S.A.* **2012**, *109*, 16073–16078.
- (32) Jung, S.; Tiwari, M. K.; Doan, N. V.; Poulikakos, D. Mechanism of Supercooled Droplet Freezing on Surfaces. *Nat. Commun.* **2012**, *3*, 615.
- (33) Kulinich, S. A.; Farzaneh, M. On Ice-Releasing Properties of Rough Hydrophobic Coatings. *Cold Reg. Sci. Technol.* **2011**, *65*, 60–64.
- (34) Rahman, M. A.; Jacobi, A. M. Drainage of Frost Melt Water from Vertical Brass Surfaces with Parallel Microgrooves. *Int. J. Heat Mass Transfer* **2012**, *55*, 1596–1605.
- (35) Lee, J. M.; Kim, B. I. Thermal Dewetting of Pt Thin Film: Etch-Masks for the Fabrication of Semiconductor Nanostructures. *Mater. Sci. Eng., A* **2007**, *449*–451, 769–773.
- (36) Buch, V.; Sandler, P.; Sadlej, J. Simulations of H<sub>2</sub>O Solid, Liquid, and Clusters, with an Emphasis on Ferroelectric Ordering Transition in Hexagonal Ice. *J. Phys. Chem. B* **1998**, *102*, 8641–8653.
- (37) Plimpton, S. Fast Parallel Algorithms for Short-Range Molecular Dynamics. *J. Comput. Phys.* **1995**, *117*, 1–19.

- (38) Brown, W. M.; Wang, P.; Plimpton, S. J.; Tharrington, A. N. Implementing Molecular Dynamics on Hybrid High Performance Computers - Short Range Forces. *Comput. Phys. Commun.* **2011**, *182*, 889–911.
- (39) Brown, W. M.; Kohlmeyer, A.; Plimpton, S. J.; Tharrington, A. N. Implementing Molecular Dynamics on Hybrid High Performance Computers - Particle-Particle Particle-Mesh. *Comput. Phys. Commun.* **2012**, *183*, 449–459.
- (40) Yeh, I. C.; Berkowitz, M. L. Ewald Summation for Systems with Slab Geometry. *J. Chem. Phys.* **1999**, *111*, 3155–3162.
- (41) Nguyen, T. D.; Carrillo, J. M. Y.; Dobrynin, A. V.; Brown, W. M. A Case Study of Truncated Electrostatics for Simulation of Polyelectrolyte Brushes on GPU Accelerators. *J. Chem. Theory Comput.* **2013**, *9*, 73–83.
- (42) Jing, T.; Kim, Y.; Lee, S.; Kim, D.; Kim, J.; Hwang, W. Frosting and defrosting on rigid superhydrophobic surface. *Appl. Surf. Sci.* **2013**, *276*, 37–42.
- (43) Rykaczewski, K.; Landin, T.; Walker, M. L.; Scott, J. H. J.; Varanasi, K. K. Direct Imaging of Complex Nano- to Microscale Interfaces Involving Solid, Liquid, and Gas Phases. *ACS Nano* **2012**, *6*, 9326–9334.
- (44) Ensikat, H. J.; Schulte, A. J.; Koch, K.; Barthlott, W. Droplets on Superhydrophobic Surfaces: Visualization of the Contact Area by Cryo-Scanning Electron Microscopy. *Langmuir* **2009**, *25*, 13077–13083.
- (45) Pokroy, B.; Kang, S. H.; Mahadevan, L.; Aizenberg, J. Self-Organization of a Mesoscale Bristle into Ordered, Hierarchical Helical Assemblies. *Science* **2009**, *323*, 237–240.
- (46) He, M.; Zhou, X.; Zeng, X.; Cui, D.; Zhang, Q.; Chen, J.; Li, H.; Wang, J.; Cao, Z.; Song, Y.; Jiang, L. Hierarchically Structured Porous Aluminum Surfaces for High-Efficient Removal of Condensed Water. *Soft Matter* **2012**, *8*, 2680–2683.
- (47) Miljkovic, N.; Enright, R.; Nam, Y.; Lopez, K.; Dou, N.; Sack, J.; Wang, E. N. Jumping-Droplet-Enhanced Condensation on Scalable Superhydrophobic Nanostructured Surfaces. *Nano Lett.* **2013**, *13*, 179–187.
- (48) Shang, H. M.; Wang, Y.; Limmer, S. J.; Chou, T. P.; Takahashi, K.; Cao, G. Z. Optically Transparent Superhydrophobic Silica-Based Films. *Thin Solid Films* **2005**, *472*, 37–43.
- (49) Extrand, C. W.; Moon, S. I. Contact Angles of Liquid Drops on Super Hydrophobic Surfaces: Understanding the Role of Flattening of Drops by Gravity. *Langmuir* **2010**, *26*, 17090–17099.
- (50) Seemann, R.; Herminghaus, S.; Jacobs, K. Dewetting Patterns and Molecular Forces: A Reconciliation. *Phys. Rev. Lett.* **2001**, *86*, 5534–5537.
- (51) Castrejon-Pita, A. A.; Castrejon-Pita, J. R.; Hutchings, I. M. Breakup of Liquid Filaments. *Phys. Rev. Lett.* **2012**, *108*, 074506.
- (52) Bischof, J.; Scherer, D.; Herminghaus, S.; Leiderer, P. Dewetting Modes of Thin Metallic Films: Nucleation of Holes and Spinodal Dewetting. *Phys. Rev. Lett.* **1996**, *77*, 1536–1539.
- (53) Fowlkes, J.; Horton, S.; Fuentes-Cabrera, M.; Rack, P. D. Signatures of the Rayleigh-Plateau Instability Revealed by Imposing Synthetic Perturbations on Nanometer-Sized Liquid Metals on Substrates. *Angew. Chem., Int. Ed.* **2012**, *51*, 8768–8772.
- (54) Furmidge, C. G. L. Studies at Phase Interfaces I. The Sliding of Liquid Drops on Solid Surfaces and a Theory for Spray Retention. *J. Colloid Sci.* **1962**, *17*, 309–324.
- (55) Reyssat, M.; Quere, D. Contact Angle Hysteresis Generated by Strong Dilute Defects. *J. Phys. Chem. B* **2009**, *113*, 3906–3909.
- (56) Karmouch, R.; Ross, G. G. Experimental Study on the Evolution of Contact Angles with Temperature Near the Freezing Point. *J. Phys. Chem. C* **2010**, *114*, 4063–4066.
- (57) He, M.; Li, H.; Wang, J.; Song, Y. Superhydrophobic Surface at Low Surface Temperature. *Appl. Phys. Lett.* **2011**, *98*, 093118.
- (58) Berendsen, H. J. C.; Grigera, J. R.; Straatsma, T. P. The Missing Term in Effective Pair Potentials. *J. Phys. Chem.* **1987**, *91*, 6269–6271.
- (59) Werder, T.; Walther, J. H.; Jaffe, R. L.; Halicioglu, T.; Koumoutsakos, P. On the Water-Carbon Interaction for Use in Molecular Dynamics Simulations of Graphite and Carbon Nanotubes. *J. Phys. Chem. B* **2003**, *107*, 1345–1352.
- (60) Vega, C.; Sanz, E.; Abascal, J. L. F. The Melting Temperature of the Most Common Models of Water. *J. Chem. Phys.* **2005**, *122*, 114507.
- (61) Conde, M. M.; Vega, C.; Patrykiewicz, A. The Thickness of a Liquid Layer on the Free Surface of Ice as Obtained From Computer Simulation. *J. Chem. Phys.* **2008**, *129*, 014702.